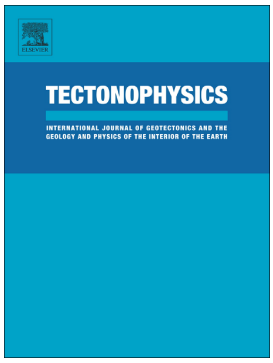

Evaluating roughness scaling properties of natural active fault surfaces by means of multi-view photogrammetry

Amerigo Corradetti, Ken McCaffrey, Nicola De Paola, Stefano Tavani

PII: S0040-1951(17)30342-6
DOI: doi: 10.1016/j.tecto.2017.08.023
Reference: TECTO 127597

To appear in: *Tectonophysics*

Received date: 15 February 2017
Revised date: 7 June 2017
Accepted date: 19 August 2017

Please cite this article as: Amerigo Corradetti, Ken McCaffrey, Nicola De Paola, Stefano Tavani , Evaluating roughness scaling properties of natural active fault surfaces by means of multi-view photogrammetry, *Tectonophysics* (2017), doi: 10.1016/j.tecto.2017.08.023

Evaluating roughness scaling properties of natural active fault surfaces by means of multi-view photogrammetry

Amerigo Corradetti[1*], Ken McCaffrey[2], Nicola De Paola[2] & Stefano Tavani[1]

1 DiSTAR, Università di Napoli, Largo San Marcellino 10, 80138 Napoli, Italy;

*amerigo.corradetti@unina.it

2 Department of Earth Sciences, Durham University, Durham, UK

Key words: Photogrammetry, Fault roughness, active faults, FFT power spectrum

Abstract

Fault roughness is a measure of the dimensions and distribution of fault asperities, which can act as stress concentrators affecting fault frictional behaviour and the dynamics of rupture propagation. Studies aimed at describing fault roughness require the acquisition of extremely detailed and accurate datasets of fault surface topography. Fault surface data have been acquired by methods such as LiDAR, laser profilometers and white light interferometers, each covering different length scales and with only LiDAR available in the field. Here we explore the potential use of multi-view photogrammetric methods in fault roughness studies, which are presently underexplored and offer the advantage of detailed data acquisition directly in the field. We applied the photogrammetric method to reproduce fault topography, by using seven dm-sized fault rock samples photographed in the lab, three fault surfaces photographed in the field, and one control object used to estimate the model error. We studied these topographies estimating their roughness scaling coefficients through a Fourier power spectrum method. Our results show scaling coefficients of 0.84±0.17 along the slip direction

and 0.91±0.17 perpendicularly to it, and are thus comparable to those results obtained by previous authors. This provides encouragement for the use of photogrammetric methods for future studies, particularly those involving field-based acquisition, where other techniques have limitations.

1. Introduction

Studies aimed at establishing the importance of fault asperity dimensional properties soon recognized that fault surface topographies display a form of self-affine behavior, i.e. different scaling occurs along the slip direction and perpendicularly to it (e.g. Mandelbrot, 1985; Brown, 1987; Thompson and Brown, 1991; Power and Tullis, 1991; Schmittbuhl et al., 1993; Lee and Bruhn, 1996). In 3D, a surface exhibiting self-affine behavior is a Z(X,Y) surface that can be described by the scaling transformation $\lambda Z(X,Y) = Z(\lambda^{1/Hx}X, \lambda^{1/Hy}Y)$ (e.g. Candela et al., 2009), where H_x and H_y are the scaling exponents, or Hurst exponents, along the X and Y direction, respectively. Since those exponents cannot be measured directly from topographic profiles of fault surfaces (e.g. Sapozhnikov and Foufoula-Georgiou, 1995), several different analytical methods have been proposed over the years for their estimation. Amongst these, the Fourier power spectrum method has proved to be the most reliable (e.g. Sagy et al., 2007; Candela et al., 2012, 2009, Bistacchi et al., 2011; Renard et al., 2013, 2012; Davidesko et al., 2014). The Fourier power spectrum *P(k)* (i.e. the square of the modulus of the Fourier transform, Schuster, 1898) of a 1D fault profile Z(X) is routinely calculated as a function of the wavenumber *k*. After plotting the Fourier power spectrum as a function of *k* in a bi-logarithmic scale graph, a self-affine function exhibits a linear slope, which is itself a function of the Hurst exponent through the relation $P(k) \propto k^{-1-2H}$. A spectrum representing the entire rough surface in a certain direction is given by stacking several power spectra and averaging them to reduce noise associated with single profiles. By using this approach, previous authors were able to observe that fault roughness, represented by the size distribution of asperities, scales over several length scales

with two distinct Hurst exponents in both the slip parallel and perpendicular directions (e.g. Candela et al., 2012). Observations made at micro-metric and nano-metric scales, by means of atomic force microscopy (ATM), have shown, however, that anisotropy is not observed below the micro-metric scale and that roughness is not self-affine at all scales being smoother at the nano-metric scale (Siman-Tov et al., 2013). More recently, Candela and Brodsky (2016) showed that the transition to isotropic roughness occurs at about 4-500 μm and interpreted this transitions as a change in the deformation mode of the asperities which, at smaller scale, appear to yield plastically losing the grooving capability.

Previous pioneering studies were affected by the poor resolution of the tools used to acquire the fault roughness dimensions, which was typically done along 1D Z(X) profiles. Nowadays, it is possible to use many accurate technologies to acquire detailed topographies. In fault roughness evaluation, for example, advances using LiDAR, laser profilometers and white light interferometers (e.g. Candela et al., 2009; Renard et al., 2013) have been achieved. These techniques, however, require sampling of the fault surface in the laboratory, except for LiDAR that is anyway unsuitable at smaller scale. An alternative, outcrop conservative and portable technique, which could open the way to the construction of high-resolution fault surface models directly in the field, involves the use of image-based 3D models. In spite of the increasing use of photogrammetrical methods in earth sciences (James and Robson, 2012; Bistacchi et al., 2015; Reitman et al., 2015; Vollgger and Cruden, 2016), the potential application of this method to the field of fault surface roughness is relatively underexplored. Photogrammetry, and particularly the algorithms involved in the digital reproduction of objects by means of photographs (i.e. SfM, Structure from Motion, Snavely et al., 2008) has experienced rapid growth during the last decades. These progresses have been encouraged by the rapid increase in hardware capability and software availability (e.g. Chandler, 1999). The application of photogrammetry allows us to produce accurate and detailed point clouds of geological outcrops as demonstrated by recent studies (Fonstad et al., 2013; Bemis et al., 2014; Tavani et al., 2016;

Wilkinson et al., 2016). However, the methods still require testing of its potential and resolution, when used to examine fault roughness scaling.

In this study, the photogrammetric method was used to acquire very detailed profiles of seven fault rock hand specimen samples, which were collected from the main slip surfaces of active normal faults in the Central Apennines of Italy (Fig.1a, Ghisetti and Vezzani, 1999, Tondi, 2000, Agosta and Aydin, 2006). In order to calibrate the methods and test its applicability in the field to natural fault surfaces, four additional fault surface models were produced. The first one was produced using a piece of graph paper, representing a control object, with similar size as the seven fault rock samples. The other three models were captured directly in the field using photographs of a natural fault surface.

The accuracy of the results was investigated by testing the self-affinity of these fault surfaces following procedures already described by other authors (e.g. Candela et al., 2012, 2009; Bistacchi et al., 2011; Renard et al., 2013) and applied to datasets obtained by means of laser scanners, laser profilometers and by white light interferometers. In addition, we tested error estimate, repeatability and reproducibility of the results.

2. Fault topography data acquisition

A set of hand specimen carbonate fault surfaces (Fig. 1 b-c) collected in the Central Apennines (Fig. 1a), were used in this study. This area of the Apennines is characterized by active normal faulting which commenced in the Late Pliocene/Early Pleistocene (Bosi and Messina, 1991), which is superimposed on a contractional edifice of the Apennine fold and thrust belt (Bigi et al., 1989). The samples belong to the sedimentary rocks of the Upper Jurassic-Lower Cretaceous Lazio-Abruzzi carbonate platform domain. All samples were collected from the principal slip zone (Smith et al., 2011) for each of these active normal faults. These samples are made of a cataclastic matrix where slip is localized along either striated or polished (mirror-like) fault slip surfaces.

The fault samples were photographed in the laboratory from viewpoints spanning 360° (Fig. 2) to produce point clouds with relatively constant density in any direction. The photographs were taken using an entry level Canon EOS 1100D with EF-S 18-55mm lens and 12.2 Mpixels, at a distance of about 30-50cm, depicting areas ranging from about 6 x 4 to 60 x 40 cm, resulting in an approximate image resolution between about 50 and 5000 pixel/mm^2. It was necessary to use a tripod to hold the camera still in order to use higher f/stops (hence smaller apertures and longer acquisition time) which helped to sharpen the background increasing the depth of field. Low ISOs were also used to further increase exposure time. Since the position of at least three points in space is necessary to scale the derived model, the rocks were photographed over a piece of graph paper (a cutting mat can also be used), where distances in the X-Y plane are easily obtained through the grid. Z is set to be 0 all along the grid so a rigid support was necessary. The graph paper alone was also photographed, using the same acquisition procedure, and it was used as a control object to assess the error in the models. In addition, three 20 x 20 cm-sized areas from the mirror of the Fiamignano Fault (Bigi and Costa Pisani, 2005; Smeraglia et al., 2016), central Apennines, were directly photographed in the field (Fig. 3a), using the same apparatus and procedure as described above, with the exception that photographs were taken along vertical strips in front of the fault wall and a rigid ruler was used for scale.

Extremely dense point clouds for the fault surfaces (Fig. 3b) and the control object (Fig. 4a) were built using the Agisoft Photoscan commercial software. The construction method (e.g. Tavani et al., 2016, 2014) performs an automatic computation of the parameters that relate the XYZ position of a point in space to its X^nY^n position in the n^{th} photograph. A denser point cloud is then generally built through pair-wise depth map computation (i.e. an image that contains information relating to the distance of surfaces belonging to scene objects from a viewpoint) or Multi-View Stereo (MVS) matching methods (i.e. specific algorithms designed to manipulate ultra-high resolution images by decomposition of the initial images to efficiently compute dense 3D point clouds). The re-scaling of the point clouds was then possible using three points picked on the graph paper or the rigid ruler as

reference (Fig. 2 and Fig. 3b). Following this procedure, we built thirteen point clouds made of about 10,000,000 points (i.e. seven fault surfaces from the collected samples, five in the field from the Fiamignano fault and one from the control object). The average area of the fault surfaces is 1100 cm^2, thus resulting in a point density spanning between 10 and 300 pts/mm^2 with an average of 150 pts/mm^2. These values are in line with previous results (e.g. Tavani et al., 2016), in which the resolution of the point cloud is about one to two orders of magnitude lower than the resolution of the input photographs. For the three photographed areas of the Fiamignano fault, we produced five point clouds in total, i.e. two clouds for the first two areas, and three clouds at different resolution for the remaining area. These experiments at the Fiamignano location were performed to test whether and to what extent the model resolution would affect the results obtained.

A major issue encountered when building models by means of multi-view photogrammetry is definition of the error, which is not intrinsically defined (e.g. Tavani et al., 2016). In order to constrain reliable value for our models, we modeled a piece of graph paper, which we assume to be perfectly planar. As previously mentioned, the photographs used to build the graph paper model have the same characteristics, including resolution and camera distance from the target object, as those used to build the faults models. Once the graph paper model was built and scaled (Fig. 4a), a best fit plane was computed and the model re-oriented and re-centred, in order to let the XY plane to coincide with the best fit plane, and the centroid of the cloud to be the origin of the reference system. Accordingly, in this new reference system, the Z value of each point defines its distance from the ideal horizontal plane corresponding to the graph paper. The frequency distribution of Z is shown in figure 4b. Such a distribution has a standard deviation of 89.1 μm, which is therefore assumed to be the models' error.

3. Fourier Power Spectrum (PFS) analysis method

A square subarea of each point cloud of the fault samples produced by means of Agisoft was imported in Matlab as a 3-D [XYZ] matrix. The original coordinate system is initially set onto the graph paper or the ruler, so that roughness is not ideally perpendicular to the fault plane (Fig. 5a-b). A change of coordinate system is necessary to set the Z coordinate perpendicular to the best fit plane of the fault surface (Fig. 5a). The new X and Y axes are arbitrarily set and an additional rotation about the Z axis is then achieved, to align the X and Y directions parallel and orthogonal to the direction of slip respectively (Fig. 5c). Minor distortion resulting from these rotations was evaluated by comparing the new Z values with the residual distances; discrepancies were found in the order of 10^{-15} m. The new matrix was split to a 2D (XY) matrix plus a 1D (Z) vector in a similar manner to previous authors (e.g. Renard et al., 2006; Sagy et al., 2007).

The next step consisted of the Fast Fourier Transform (FFT) analysis. The XY matrixes built in the previous steps have irregularly spaced coordinates, while a regular grid is needed for the FFT algorithm. A new set of regularly spaced grids defined by spacing twice as large as the average irregular spacing of the original point clouds was hence defined. The corresponding linearly interpolated Z values were stored in a MXN matrix, where M and N are the number of resampled points along the slip and the slip-perpendicular directions of the fault, respectively. The FFT analysis through the interpolated surfaces was then achieved using a 1D FFT approach (e.g. Renard et al., 2013). In essence, each row and then each column of each grid that stores the interpolated Z values is extracted and analyzed independently in the XZ and YZ spaces (Fig. 6). For each grid, the results of all the FFT-derived power spectra, computed along the X direction, were graphed together in a *k* vs *P(k)* plot (Fig. 7), where *k* is the wavelength and *P(k)* is the power of the FFT. The same was done for the power spectra along the Y direction which served to remove possible bias associated with individual profiles. Interpolation of the data was done after individual *k-P(k)* profiles were averaged using regularly spaced log(k) intervals (Fig. 7).

The Matlab script used to perform the procedures described above is available upon request to the corresponding author.

4. PFS results

We reproduced the topography of ten fault mirrored surfaces from the main fault surfaces of active normal faults from the Central Apennines (Italy), and estimated their self-affine behaviour and the corresponding scaling exponents using the Fourier power spectrum method. The magnitude of the scaling behaviour (i.e. magnitude of the fault roughness) is expressed by the pre-factor of the power law (Candela et al., 2012 and references therein).

The results of our analysis are reported in Table 1 and figures 8 and 9. The seven fault samples collected in the field and photographed in laboratory are characterized by an average Hurst exponent of 0.84±0.17 along the slip direction and 0.91±0.17 perpendicularly to it (Fig. 8). Their pre-factors are characterized by four orders of magnitude of variability (Table 1). This variability is also graphically expressed by the dashed black lines in figure 8. Overall, the average pre-factor of the along-slip spectra is at least one order of magnitude smaller than the perpendicular-to-slip one (Fig. 8).

The power spectra of the additional fault surfaces from the Fiamignano fault, corresponding to the FM1, FM2, and FM3 in Table 1 yielded Hurst exponents of 0.66, 0.68 and 0.58 along the slip direction, and 0.67, 0.65 and 0.7 in the slip perpendicular direction (Fig. 9). In order to test the influence of resampling on the results, the point cloud FM1a was also resampled using different spacing consisting in 4x, 8x and 16x the mean spacing (Table 1 and Fig. 9). Both slip parallel and slip perpendicular Hurst exponents decrease with increasing spacing, showing values of 0.62, 0.56 and 0.49 along-slip and 0.62, 0.52 and 0.40 perpendicularly to it (Table 1). A further experiment consisted

of a FFT analysis of the FM1a fault (composed of about 25 million of points) produced at different resolutions (i.e. 6.1 million and 1.5 million of points). These samples (namely FM1b and FM1c in Table 1) show Hurst exponents of 0.67 and 0.62 along the slip direction (0.66 in the high-resolution model) and 0.65 and 0.59 perpendicularly to it (0.67 in the high-resolution model), respectively. The variability of the pre-factors for the three Fiamignano fault patches (table 1 and Fig. 9) is within one order of magnitude, with the along-slip pre-factor value about one order of magnitude smaller than the one calculated perpendicular to slip (Fig. 9).

5. Discussion

A series of fault topographies have been acquired by means of multi-view photogrammetry with the aim of demonstrating the potential of this technique in reproducing sub-millimeter scale roughness. Standard in situ acquisition techniques, such as laser scanners, have a noise of about 0.2 to 1 cm in the direction of scanning (e.g. Candela et al., 2012), hence, these devices may be only used to study relatively larger scale anisotropies. One must resort to other methods, such as laboratory laser profilometers, to resolve roughness at these smaller scales. By contrast, the resolution of photogrammetry is strictly related to photograph resolution, making the technique a highly versatile one as it allows to obtain a broader range of scales compared to standard acquisition techniques used to date.

In spite of the wide versatility of the photogrammetric method, the main issue in common with other applications of photogrammetry is definition of the error, which is not known a priori compared to many other measuring tools. To overcome this issue, and provide a trustworthy value for the error in our models, we modeled a piece of graph paper, which we assumed to be perfectly planar. The error of the models can thus be evaluated by the standard deviation of the distances between the points

belonging to the graph paper model and their best fit plane. The error was found to be 89.1 μm (Fig. 4), which is essentially within the same order of magnitude as the models' resolution.

The results of our analysis on the seven fault samples collected in the field and photographed in laboratory showed mean values of the Hurst exponents of 0.84±0.17 along the slip direction and 0.91±0.17 perpendicularly to it (Fig. 8). These faults include both striated and polished topographies that were exposed to weathering. It is likely that this topographic variability is also responsible of the large variations observed in terms of pre-factor (Table 1). However, comparing these results with previously published work (e.g. Candela et al., 2012; Renard et al., 2013), we observe that even if we report higher values of Hurst exponents compared to those authors (e.g. about 0.6 and 0.8 in the direction of slip and perpendicular to it, respectively), our Fourier power spectra agrees in terms of magnitude of the scaling behaviour for the same investigated length scales.

By collecting and analysing three different photosets at various positions along the Fiamignano fault, we also tested the method directly in the field. The average Hurst exponents for these three fault surfaces are 0.64±0.05 along slip and 0.68±0.02 perpendicularly to slip. These slip-perpendicular values are however influenced by local low amplitude of the signals at about k = 1dm (Fig. 9). If we, for example, remove these values from the dataset, we obtain an average perpendicular to slip Hurst exponent of 0.75±0.09. These corrected values are therefore also in agreement with previous works, not only with the overall trend (i.e. fault scaling magnitude) but also in absolute terms. The weak variability observed in term of pre-factor at the Fiamignano fault patches (Fig. 9) agrees with the previous hypothesis that the strong variations observed at the seven fault samples collected in the field (Fig. 8) was caused by fault topographic variability.

For the Fiamignano fault we did two additional experiments to test whether and to what extent the model resolution and the re-sampling rate prior to FFT would affect the results. The first experiments consisted in the production of two additional point clouds obtained at different resolutions for the FM1a fault (Fig. 9). These are the FM1b and FM1c faults (Table 1). The power

spectra of these three faults overlap (Fig. 9) as indicated by the standard deviation of their Hurst exponents, which are 0.02 and 0.03 in the slip and its perpendicular direction, respectively. These results are very important because suggest that the technique is of broad and universal application as comparable results can be obtained for example using different cameras and software. The other experiment consisted in the resampling of the FM1a point cloud using different spacing consisting of 4, 8 and 16 times the mean spacing between points of the cloud, in addition to the 2 times mean spacing considered in previous experiments. Their power spectra perfectly overlap (Fig. 9). The most evident and obvious effect whit increasing spacing is that a progressively lesser short spatial frequency *k* is investigated.

In conclusion, our results show that by means of photogrammetry, it is possible to acquire very detailed point clouds of rough surfaces such as faults. In particular, it is possible to attain: 1) much more detailed on-site profiles that would be acquired by laser scanner-based methods alone, and 2) bridge the gap between LiDAR and laboratory equipment such as laser profilometers, often used to complement datasets acquired with lower resolution methods. Our results show that no significant differences exist between roughness parameters obtained by models derived in the laboratory or directly in the field. In fact, results obtained in the field fall within the variability observed in the laboratory. Overall, our results show that multi-view photogrammetry method is a versatile and universal tool for extensive and conservative data acquisition. Finally, our study also shows how high resolution roughness analysis typically available in the laboratory can now be achieved in the field.

6. Conclusions

In this study, we tested the multi-view photogrammetric technique to model the roughness of dm-sized fault surfaces and obtain their roughness parameters. Ten 3D models have been constructed, with a resolution of nearly 0.1 mm, using both rock samples photographed in the laboratory and fault

surfaces photographed directly in the field. Differences between the two sets of models are negligible, and both display a self-affine behaviour fully in agreement with previous studies carried out by means of LiDAR, laser profilometer, and white light interferometer equipment. Our data demonstrate that, in the field and for the investigated scales, photogrammetry is able to cover and improve the resolution attained by LiDAR and to bridge the gap between field-based instrument and laboratory-based laser profilometers. This allows us to conclude that multi-view photogrammetry is able to provide a viable tool for producing very detailed models of fault surfaces in a fast and cheap way that can be utilised in fieldwork.

Acknowledgements

This study was supported by the Natural Environment Research Council (NERC Standard Grant NE/H021744/1 awarded to Nicola De Paola. F. Agosta, F. Balsamo and F. Storti are thanked for providing help during fieldwork and fault surfaces sample collection.

We greatly appreciated the constructive revision and comments by an anonymous Reviewer and the Editor.

References

Agosta, F., Aydin, A., 2006. Architecture and deformation mechanism of a basin-bounding normal fault in Mesozoic platform carbonates, central Italy. J. Struct. Geol. 28, 1445–1467. doi:10.1016/j.jsg.2006.04.006.

Bemis, S.P., Micklethwaite, S., Turner, D., James, M.R., Akciz, S., Thiele, S.T., and Bangash, H.A., 2014. Ground-based and UAV-Based photogrammetry: A multi-scale, high-resolution mapping

tool for structural geology and paleoseismology: Journal of Structural Geology, v. 69, p. 163–178, doi: 10.1016/j.jsg.2014.10.007.

Bigi, G., Cosentino, D., Parlotto, M., Sartori, R., and Scandone, P., 1989. Structural model of Italy 1:500,000. Progetto Finalizzato Geodinamica: Quaderni della Ricerca Scientifica CNR, no. 114.

Bigi, S., and Costa Pisani, P., 2005. From a deformed Peri-Tethyan carbonate platform to a fold-and-thrust-belt: an example from the Central Apennines (Italy): Journal of Structural Geology, v. 27, no. 3, p. 523–539, doi: 10.1016/j.jsg.2004.10.005

Bistacchi, A., Balsamo, F., Storti, F., Mozafari, M., Swennen, R., Solum, J., Tueckmantel, C., and Taberner, C., 2015. Photogrammetric digital outcrop reconstruction, visualization with textured surfaces, and three-dimensional structural analysis and modeling: Innovative methodologies applied to fault-related dolomitization (Vajont Limestone, Southern Alps, Italy): Geosphere, p. GES01005.1, doi: 10.1130/GES01005.1.

Bistacchi, A., Griffith, W.A., Smith, S.A.F., Di Toro, G., Jones, R.R., and Nielsen, S., 2011. Fault Roughness at Seismogenic Depths from LIDAR and Photogrammetric Analysis: Pure and Applied Geophysics, v. 168, no. 12, p. 2345–2363, doi: 10.1007/s00024-011-0301-7.

Bosi, C., Messina, P., 1991. Ipotesi di correlazione fra successioni morfo-litostratigrafiche plio-pleistoceniche nell'Appennino Laziale-Abruzzese. Stud. Geol. Camerti 2, 257–263.

Brown, S.R., 1987. A note on the description of surface roughness using fractal dimension: Geophysical Research Letters, v. 14, no. 11, p. 1095–1098, doi: 10.1029/GL014i011p01095.

Candela, T., Brodsky, E.E., 2016. The minimum scale of grooving on faults. Geology, v. 44, p. 603–606, doi:10.1130/G37934.1.

Candela, T., Renard, F., Bouchon, M., Brouste, A., Marsan, D., Schmittbuhl, J., and Voisin, C., 2009.

Characterization of Fault Roughness at Various Scales: Implications of Three-Dimensional High Resolution Topography Measurements: Pure and Applied Geophysics, v. 166, no. 10–11, p. 1817–1851, doi: 10.1007/s00024-009-0521-2.

Candela, T., Renard, F., Klinger, Y., Mair, K., Schmittbuhl, J., and Brodsky, E.E., 2012. Roughness of fault surfaces over nine decades of length scales: Journal of Geophysical Research, v. 117, no. B8, p. B08409, doi: 10.1029/2011JB009041.

Chandler, J., 1999. Effective application of automated digital photogrammetry for geomorphological research: Earth Surface Processes and Landforms, v. 24, no. 1, p. 51–63, doi: 10.1002/(SICI)1096-9837(199901)24:1<51::AID-ESP948>3.0.CO;2-H.

Davidesko, G., Sagy, A., Hatzor, Y.H., 2014. Evolution of slip surface roughness through shear. Geophys. Res. Lett. 41, 1492–1498. doi:10.1002/2013GL058913

Fonstad, M.A., Dietrich, J.T., Courville, B.C., Jensen, J.L., and Carbonneau, P.E., 2013. Topographic structure from motion: a new development in photogrammetric measurement: Earth Surface Processes and Landforms, v. 38, no. 4, p. 421–430, doi: 10.1002/esp.3366.

Ghisetti, F., and Vezzani, L., 1999. Depth and modes of Pliocene-Pleistocene crustal extension of the Apennines (Italy): Terra Nova, v. 11, no. 2–3, p. 67–72, doi: 10.1046/j.1365-3121.1999.00227.x.

James, M.R., and Robson, S., 2012. Straightforward reconstruction of 3D surfaces and topography with a camera: Accuracy and geoscience application: Journal of Geophysical Research, v. 117, no. F3, p. F03017, doi: 10.1029/2011JF002289.

Lee, J., Bruhn, R., 1996. Structural anisotropy of normal fault surfaces. J. Struct. Geol.

Mandelbrot, B.B., 1985. Self-Affine Fractals and Fractal Dimension: Physica Scripta, v. 32, no. 4, p. 257–260, doi: 10.1088/0031-8949/32/4/001.

Power, W.L., and Tullis, T.E., 1991. Euclidean and fractal models for the description of rock surface roughness: Journal of Geophysical Research, v. 96, no. B1, p. 415, doi: 10.1029/90JB02107.

Reitman, N.G., Bennett, S.E.K., Gold, R.D., Briggs, R.W., and DuRoss, C.B., 2015. High-Resolution Trench Photomosaics from Image-Based Modeling: Workflow and Error Analysis: Bulletin of the Seismological Society of America, v. 105, no. 5, p. 2354–2366, doi: 10.1785/0120150041.

Renard, F., Candela, T., and Bouchaud, E., 2013. Constant dimensionality of fault roughness from the scale of micro-fractures to the scale of continents: Geophysical Research Letters, v. 40, no. 1, p. 83–87, doi: 10.1029/2012GL054143.

Renard, F., Mair, K., and Gundersen, O., 2012. Surface roughness evolution on experimentally simulated faults: Journal of Structural Geology, v. 45, p. 101–112, doi: 10.1016/j.jsg.2012.03.009.

Renard, F., Voisin, C., Marsan, D., and Schmittbuhl, J., 2006. High resolution 3D laser scanner measurements of a strike-slip fault quantify its morphological anisotropy at all scales: Geophysical Research Letters, v. 33, no. 4, p. L04305, doi: 10.1029/2005GL025038.

Sagy, A., Brodsky, E.E., and Axen, G.J., 2007. Evolution of fault-surface roughness with slip: Geology, v. 35, no. 3, p. 283, doi: 10.1130/G23235A.1.

Sapozhnikov, V., and Foufoula-Georgiou, E., 1995. Study of self-similar and self-affine objects using logarithmic correlation integral: Journal of Physics A: Mathematical and General, v. 28, no. 3, p. 559–571, doi: 10.1088/0305-4470/28/3/012.

Schmittbuhl, J., Gentier, S., and Roux, S., 1993. Field measurements of the roughness of fault surfaces: Geophysical Research Letters, v. 20, no. 8, p. 639–641, doi: 10.1029/93GL00170.

Schuster, A., 1898. On the investigation of hidden periodicities with application to a supposed 26 day

period of meteorological phenomena: Journal of Geophysical Research, v. 3, no. 1, p. 13, doi: 10.1029/TM003i001p00013.

Siman-Tov, S., Aharonov, E., Sagy, A., and Emmanuel, S., 2013. Nanograins form carbonate fault mirrors: Geology, v. 41, no. 6, p. 703–706, doi: 10.1130/G34087.1.

Smeraglia, L., Aldega, L., Billi, A., Carminati, E., Doglioni, C., 2016. Phyllosilicate injection along extensional carbonate-hosted faults and implications for co-seismic slip propagation: Case studies from the central Apennines, Italy. J. Struct. Geol. 93, 29–50. doi:10.1016/j.jsg.2016.10.003.

Smith, S.A.F., Billi, A., Di Toro, G., Spiess, R., 2011. Principal Slip Zones in Limestone: Microstructural Characterization and Implications for the Seismic Cycle (Tre Monti Fault, Central Apennines, Italy). Pure Appl. Geophys. 168, 2365–2393. doi:10.1007/s00024-011-0267-5.

Snavely, N., Seitz, S.M., and Szeliski, R., 2008. Modeling the world from Internet photo collections: International Journal of Computer Vision, v. 80, no. 2, p. 189–210, doi: 10.1007/s11263-007-0107-3.

Tavani, S., Corradetti, A., and Billi, A., 2016. High precision analysis of an embryonic extensional fault-related fold using 3D orthorectified virtual outcrops: The viewpoint importance in structural geology: Journal of Structural Geology, v. 86, p. 200–210, doi: 10.1016/j.jsg.2016.03.009.

Tavani, S., Granado, P., Corradetti, A., Girundo, M., Iannace, A., Arbués, P., Muñoz, J.A., and Mazzoli, S., 2014. Building a virtual outcrop, extracting geological information from it, and sharing the results in Google Earth via OpenPlot and Photoscan: An example from the Khaviz Anticline (Iran): Computers & Geosciences, v. 63, p. 44–53, doi: 10.1016/j.cageo.2013.10.013.

Thompson, M.E., and Brown, S.R., 1991. The effect of anisotropic surface roughness on flow and transport in fractures: Journal of Geophysical Research: Solid Earth, v. 96, no. B13, p. 21923–21932, doi: 10.1029/91JB02252.

Tondi, E., 2000. Geological analysis and seismic hazard in the Central Apennines (Italy). J. Geodyn. 29, 517–533. doi:10.1016/S0264-3707(99)00048-4

Vollgger, S.A., and Cruden, A.R., 2016. Mapping folds and fractures in basement and cover rocks using UAV photogrammetry, Cape Liptrap and Cape Paterson, Victoria, Australia: Journal of Structural Geology, v. 85, p. 168–187, doi: 10.1016/j.jsg.2016.02.012.

Wilkinson, M.W., Jones, R.R., Woods, C.E., Gilment, S.R., McCaffrey, K.J.W., Kokkalas, S., Long, J.J., 2016. A comparison of terrestrial laser scanning and structure-from-motion photogrammetry as methods for digital outcrop acquisition. Geosphere 12, 1865–1880. doi:10.1130/GES01342.1

CAPTIONS LIST

Figure 1

(a) Simplified tectonic scheme of the Central Apennine Downfaulted Area, with location of samples. (b) Fault surface, with detail (c), of a sampled fault.

Figure 2

Screenshots of the 3D environment of a point cloud in Agisoft Photoscan. Photographs (indicated by blue rectangles) were taken from vantage points that span 360° around the fault rock samples using a

tripod. Referencing and scaling is assured by placing a rigid sheet of graph paper. The paper is set at 0 elevation and the mesh of the graph paper is used for X and Y positioning.

Figure 3

(a) Detail of the Fiamignano fault surface and of (b) the corresponding point cloud.

Figure 4

(a) Screenshots of the 3D model of the paper sheet used to define the error. (b) Frequency histogram of the Z value of the model, representing the error.

Figure 5

(a) Procedure for the re-orientation of a fault surface from a reference system defined by the reference points on graph paper with the Z direction that is not perpendicular to the fault plane. The new coordinate system is centred at the centroid of the point cloud and the new Z direction is defined normal to the best-fit plane. (b) Image of a pre-rotation point cloud and (c) same cloud after rotation. This latter was also resampled to create a regular grid with a sampling rate twice large the average spacing of the original cloud.

Figure 6

Example of one of the analysed signal in the XZ space.

Figure 7

This graph shows the result of the along slip power spectra along one of the fault sample. 563 along slip profiles of just one fault are analysed independently and the results averaged in a geometric progression (black dots). These equidistant points (in the log scale except for the first three values) are interpolated in order to find the along slip Hurst exponent for the analysed surface.

Figure 8

In this figure, the power spectra result in the two orthogonal directions for the faults collected in the field and photographed in lab – averaged by using regularly spaced log(k) intervals – are plotted. The two dashed black lines represent power laws with parameters stated in bold. In particular, the average Hurst exponents was assigned, while two distinct pre-factors (a) are shown in each graph to visualize the variability of this parameter at the given Hurst exponent.

Figure 9

Perpendicular to slip (on top) and slip parallel (below) results of the mean Fourier power spectra performed along the point clouds of the Fiamignano fault. The dotted black lines represent power law fits with Hurst exponents that are equivalent to the mean Hurst exponent along each direction excluding the values at k > 1 dm for the perpendicular to slip power spectra. Further description is in the text.

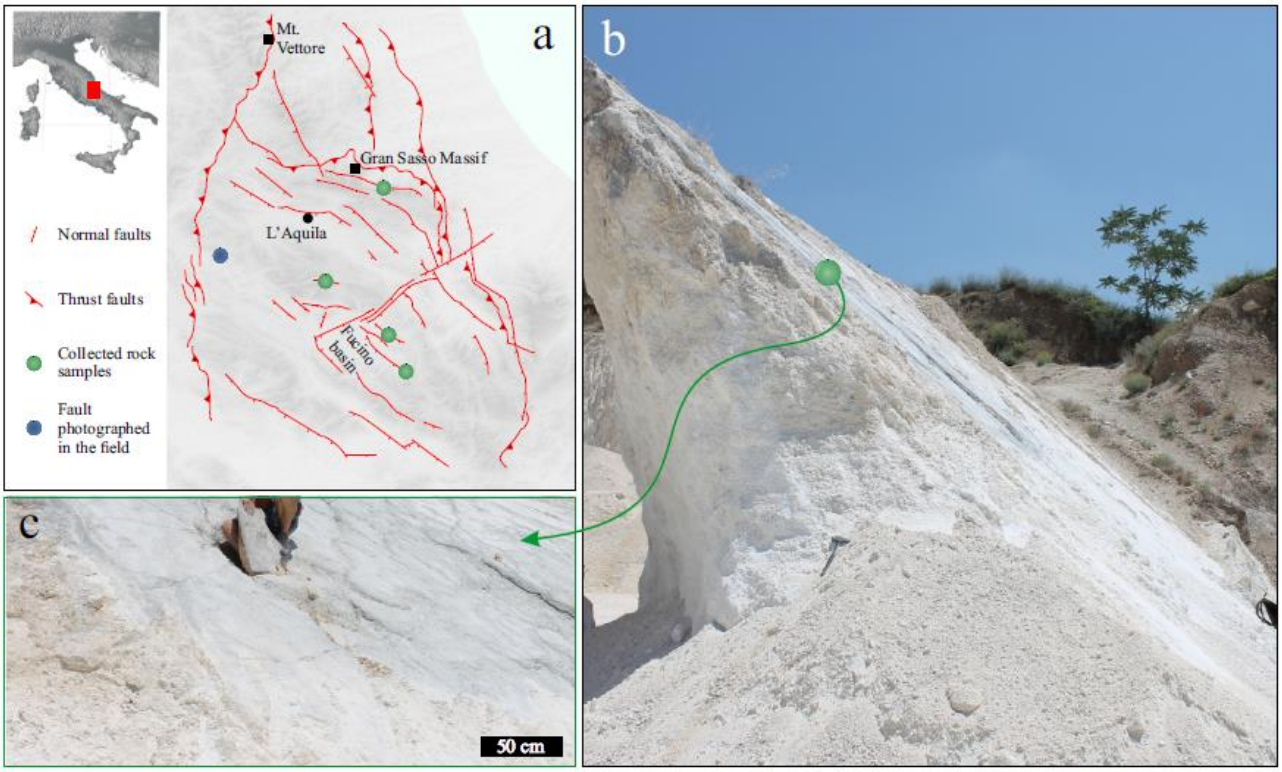

Figure 1

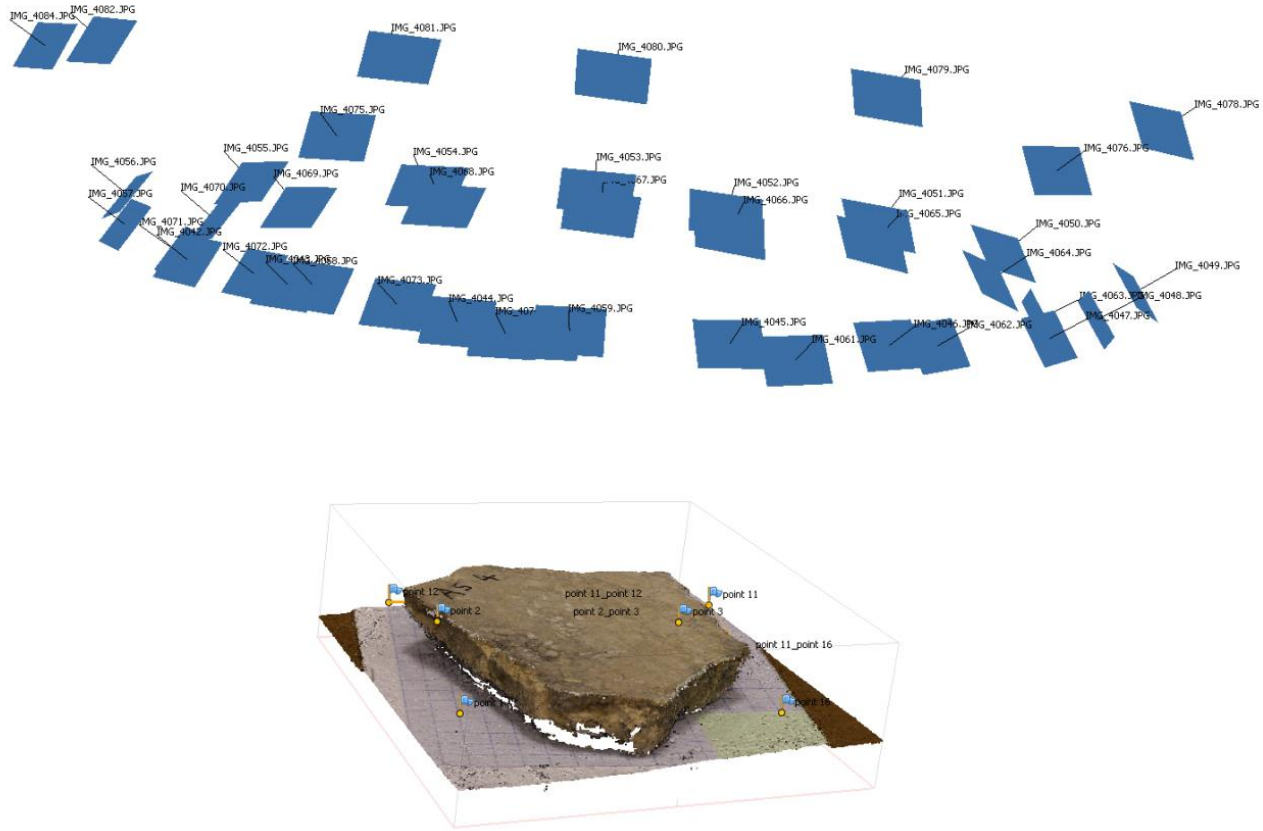

Figure 2

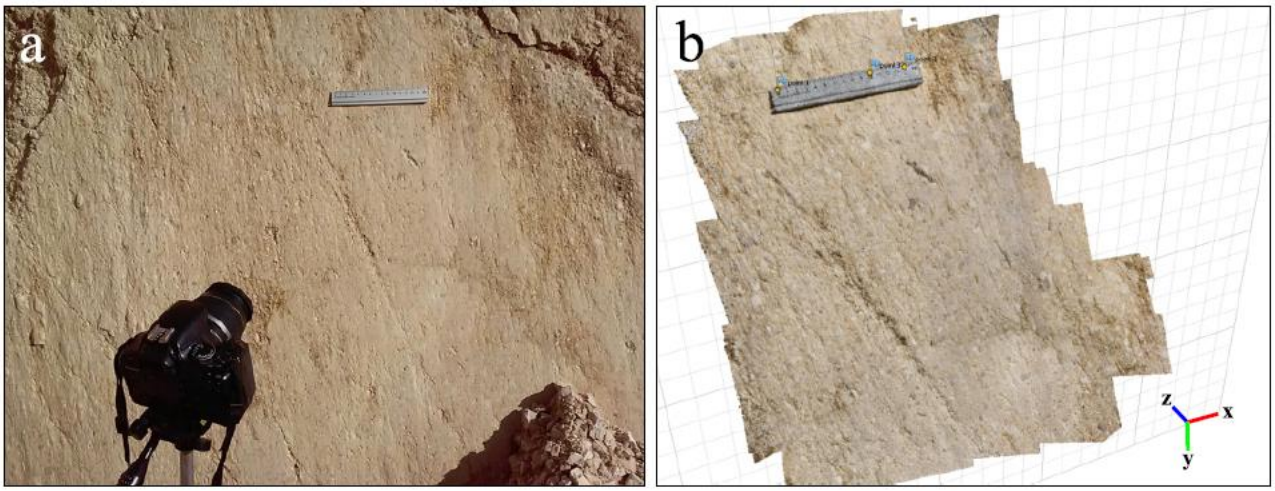

Figure 3

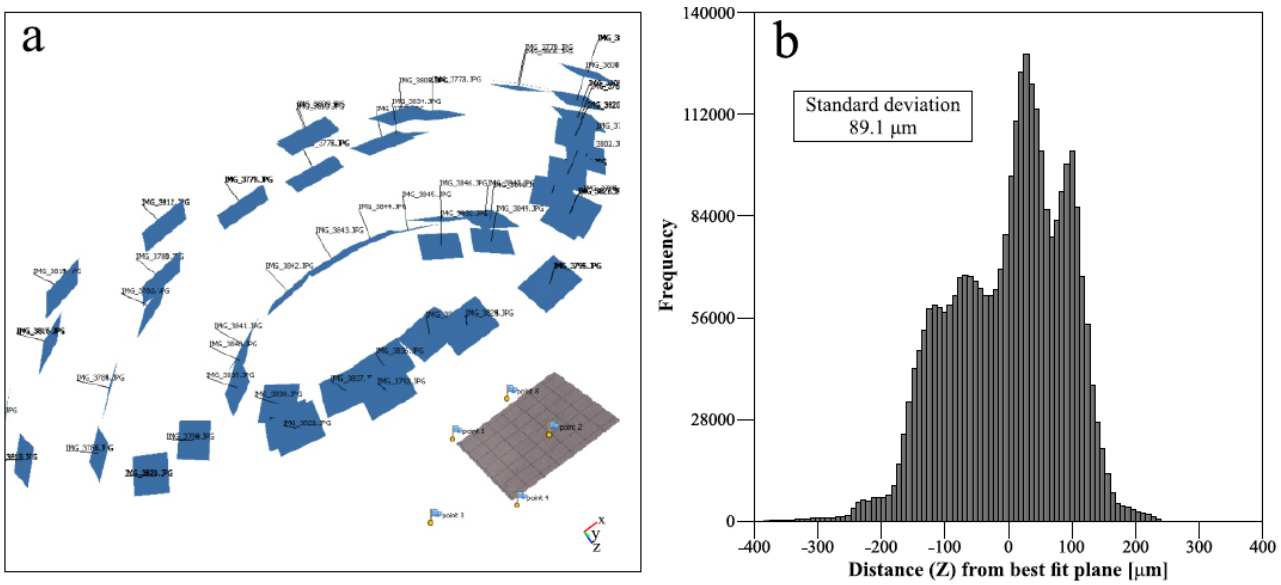

Figure 4

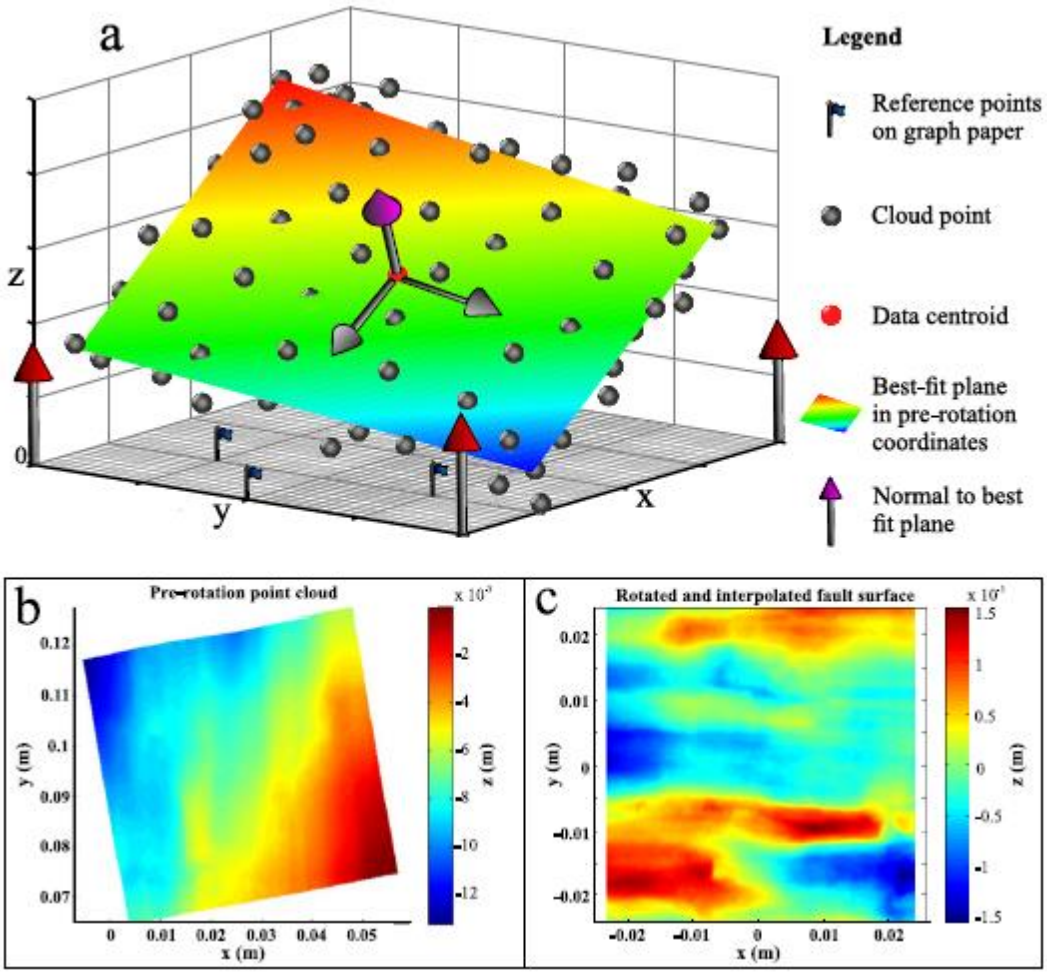

Figure 5

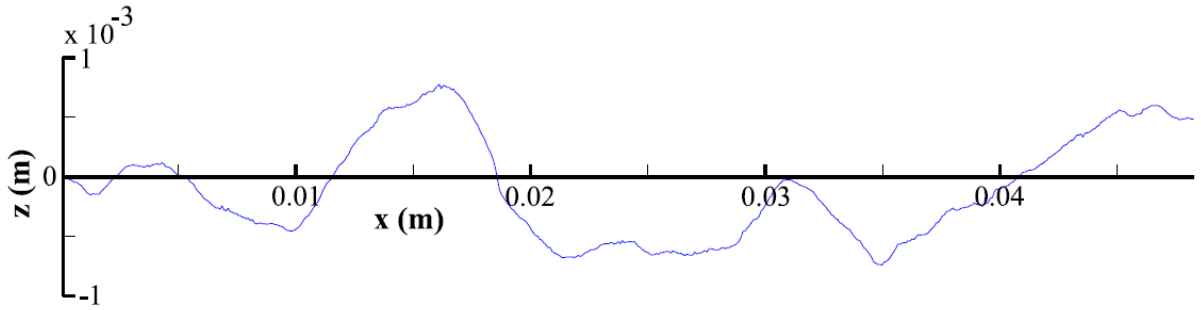

Figure 6

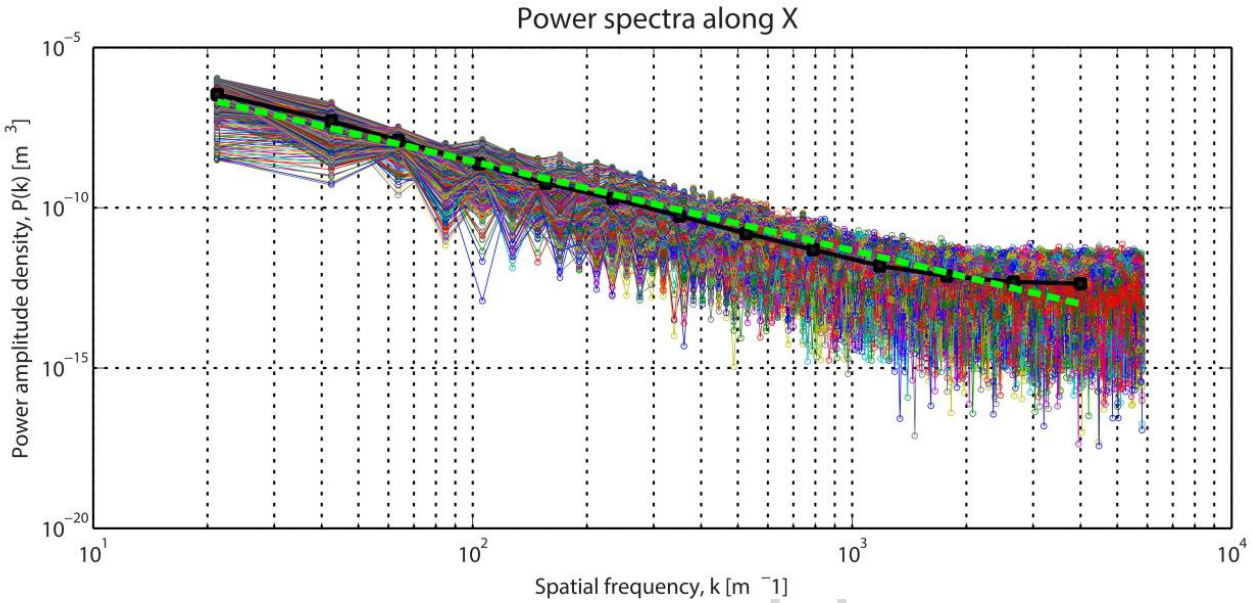

Figure 7

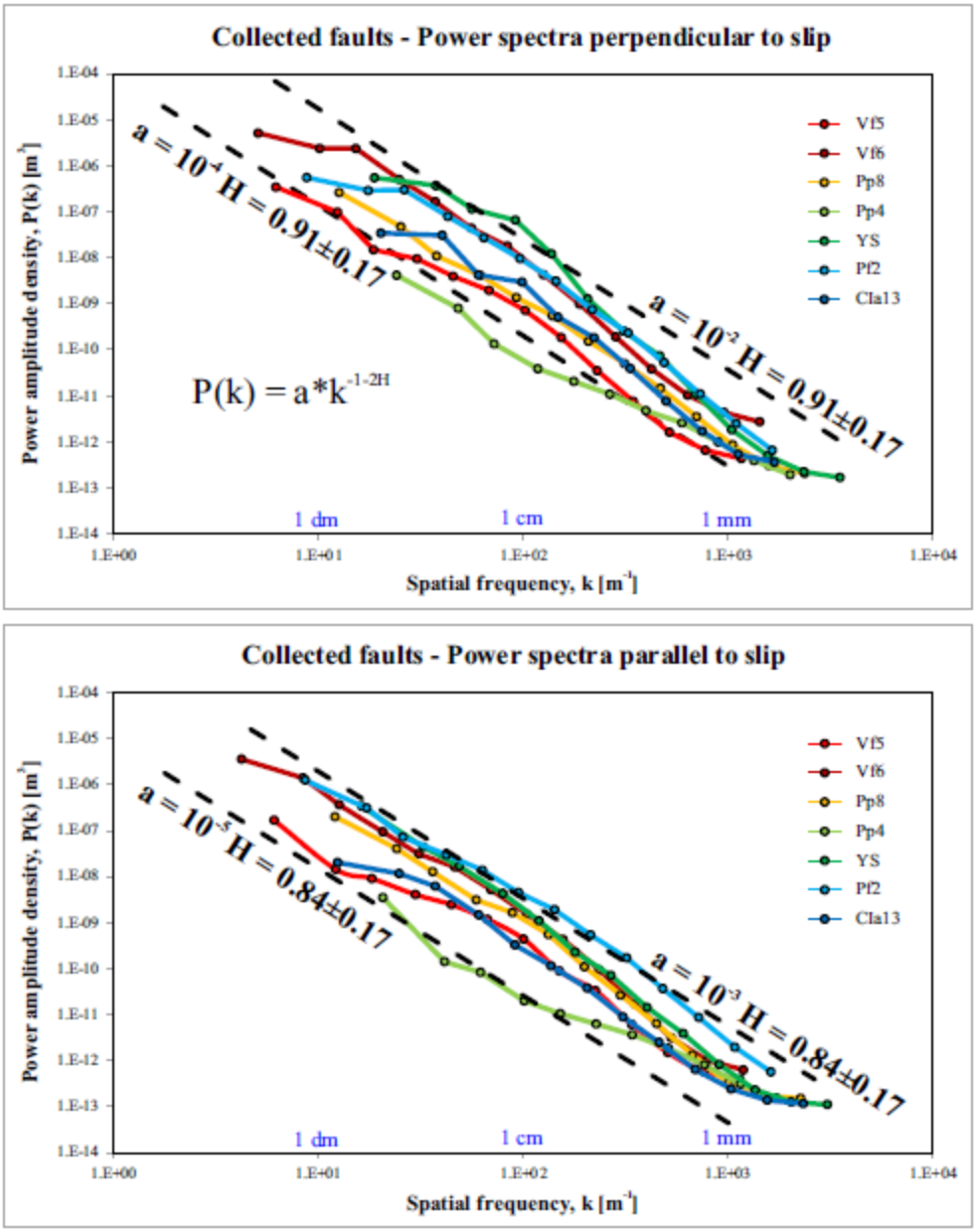

Figure 8

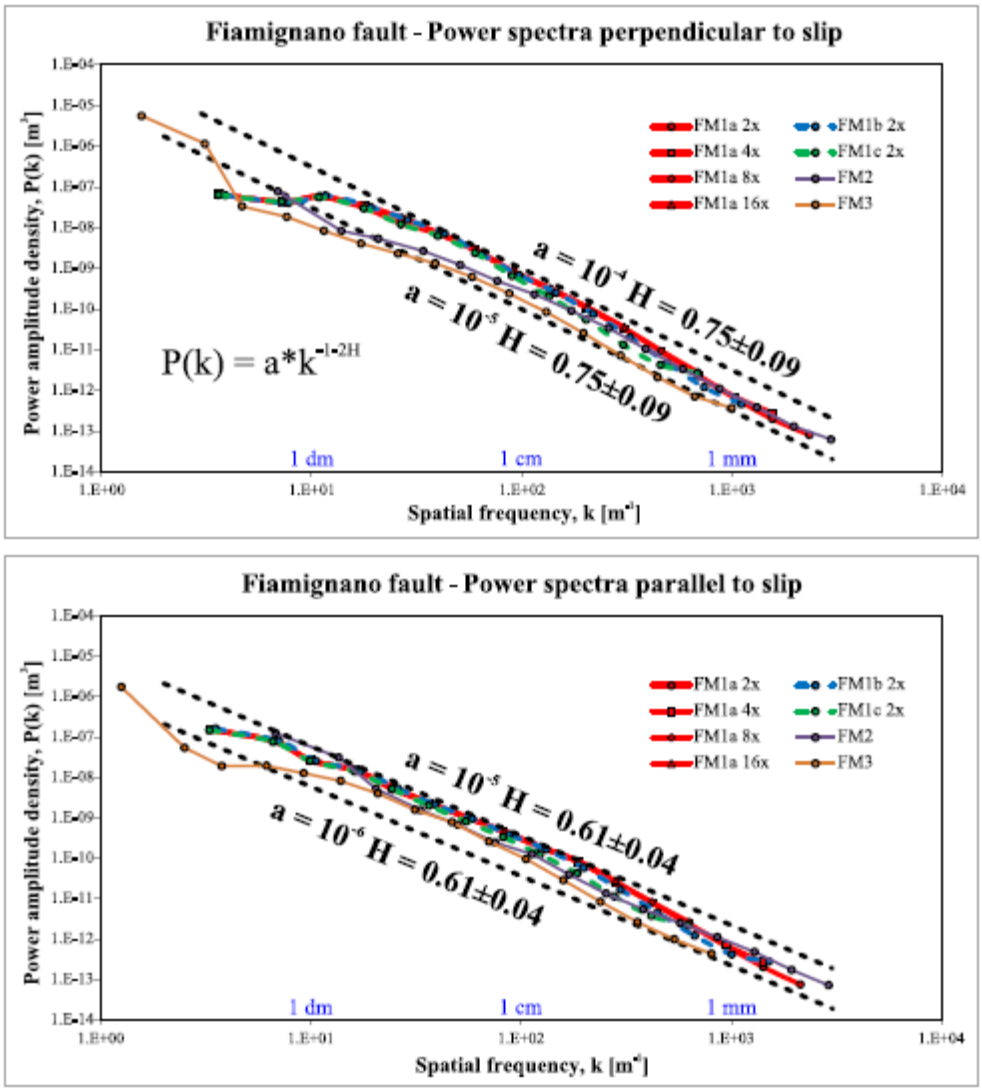

Figure 9

Table 1

Results of the FFT analysis on all points cloud. Along slip is indicated by the // symbol, while perpendicular to slip symbol is -|.

Table 1

Sample code	Number of points	Area [m2]	Points per cm2	Resampling (Mean distance)	H //	a //	R^2	H -|	a -|	R^2
VF5	2400000	0.036	6695	2x	0.76	1.0E-04	0.980	0.87	2.0E-05	0.984
VF6	3200000	0.060	5333	2x	0.97	3.1E-03	0.989	0.95	7.0E-04	0.980
PP8	1600000	0.008	20000	2x	0.90	4.0E-04	0.990	0.97	5.0E-04	0.997
PP4	1013834	0.005	22344	2x	0.48	2.0E-06	0.969	0.55	3.0E-07	0.983
YS	1349160	0.004	31720	2x	1.05	6.2E-02	0.992	1.18	2.3E-03	0.976
PF2	4160000	0.021	19810	2x	0.90	1.8E-03	0.991	0.91	1.1E-03	0.975
CIa13	1000000	0.007	14085	2x	0.83	8.0E-04	0.984	0.97	5.0E-05	0.977
FM1a	2.6E+07	0.128	20114	2x	0.66	1.0E-05	0.988	0.67	7.0E-06	0.957
FM1a	2.6E+07	0.128	20114	4x	0.62	1.0E-05	0.988	0.62	6.0E-06	0.952
FM1a	2.6E+07	0.128	20114	8x	0.56	5.0E-06	0.990	0.52	4.0E-06	0.942
FM1a	2.6E+07	0.128	20114	16x	0.49	3.0E-06	0.993	0.40	3.0E-06	0.918
FM1b	6100000	0.128	4778	2x	0.67	1.0E-05	0.989	0.65	8.0E-06	0.941
FM1c	1500000	0.128	1175	2x	0.62	7.0E-06	0.990	0.59	5.0E-06	0.941
FM2	1.1E+07	0.036	30301	2x	0.68	8.0E-06	0.996	0.66	8.0E-06	0.992
FM3	2E+07	0.746	2721	2x	0.58	6.0E-06	0.973	0.70	1.0E-06	0.979

Results of the FFT analysis on all points cloud. Along slip is indicated by the // symbol, while perpendicular to slip symbol is -|.

Highlights

- Accurate topographies of faults can be captured by means of photogrammetry
- Photogrammetry allows to bridge the gap between LiDAR and Laser profilometers
- Fault roughness can be measured directly in the field with higher detail than LiDAR